Robot Leg Motion in a Planarized-SOI, Two-Layer Poly-Si Process

Seth Hollar, Anita Flynn, Sarah Bergbreiter, *Student Member, IEEE*, and K. S. J. Pister

***Abstract*—With the ultimate goal of creating autonomous microrobots, we developed a five-mask process that combines two polysilicon structural layers with 50-μm-thick SOI structures and a backside substrate etch. The polysilicon layers provide three-dimensional (3-D) hinged structures, high compliance structures, and electrical wiring. The SOI structural layer yields much stronger structures and large-force actuators. This process was developed as a part of a three-chip solution for a solar-powered 10-mg silicon robot. Here, we describe the fabrication of this planarized-SOI, two-layer poly-Si process (henceforth called the SOI/poly process), basic modules in the design of robot legs in this process, and lastly, the results of fabricated robot legs. In designing the leg structures, we developed guidelines and test structures to provide a better understanding of the robot leg performance. These guidelines include understanding the relationship between the lateral etch depth to the actuator spacing and performing static friction tests of polysilicon flaps to more accurately model the frictional forces of the linkages. Last, we report on the performance of the robot legs and inchworm motors. On an 8 mm $\times$ 3 mm robot, we have demonstrated a 1 degree-of-freedom (DOF) robot leg, 1 mm in length, which demonstrates up to 60 μN of vertical leg force with an angular deflection of almost 30°. A two-DOF robot leg, also 1 mm in length, operated with at least 90° of angular deflection, and each inchworm motor demonstrated a shuttle displacement of 400 μm with speeds up to 6.8 mm/s. In addition to robot legs, a bidirectional inchworm motor that produces equivalent forces in both directions was also fabricated in this SOI/poly process. This motor uses an additional set of gap-closing-actuator (GCA) arrays to prebias the drive frame.**

[1305]

***Index Terms*—Electrostatic actuators, inchworm motors, microrobots.**

I. Introduction

A. Motors

UNTIL recently, one of the fundamental problems in designing autonomous microrobots has been finding actuators that are both efficient and also capable of generating large forces and displacements. A survey of some of the major actuator classes, including electromagnetic, electrostatic, thermal, shape-memory, and piezoelectric, can be found in [1]–[3]. Electromagnetics, while efficient at the macroscale, require large magnetic fields that do not fit well in a small form factor. Similarly, piezoelectrics, while offering excellent power densities [4] have not yet been easily incorporated in a micromachining process.

Researchers have demonstrated limb motion for microrobots using electrothermal and electrostatic actuation [5]–[7]. While "large" forces can be attained electrostatically with gap-closing actuators (GCAs), small displacements limit their initial usefulness. However, if two GCAs are used in an inchworm configuration, large displacements can be achieved without sacrificing the large force capability of a gap-closing electrostatic actuator. While the phrase "inchworm" was originally coined to signify a specific type of incremental piezoelectric actuator which would grab and release a shuttle and "inch" the shuttle along, the designation, "inchworm" has come to be used generically to signify a variety of actuation schemes (whether piezoelectric, thermal, or electrostatic) that convert small motions into larger motions without compromising force output.

A number of groups [8]–[10] have fabricated inchworm drives based on electrothermal actuators but their low efficiencies (10^{-7}) [10] rule them out for autonomous microrobot applications. Other groups have developed electrostatic inchworm drives to take advantage of nanometer-resolution in positioning stages [11], [12] or have focused on surface micromachining processes for electrostatic inchworm drives [13]–[15].

In our microrobot application, we are not concerned with precise nanometer stepping, but rather are focused on achieving large shuttle displacement, without trading off force, all the while working at the lowest power levels possible. Consequently, our direction has been to utilize an SOI process (to maximize output force), to use electrostatics (for efficiency) and to use gearteeth in actuator/shuttle engagement (for simplicity). The inchworm drive that we describe in this paper is composed of four sets of GCA arrays: two drive actuators and two clutch actuators. Each clutch/drive pair is used to inch the shuttle forward (Fig. 1). The clutch actuator engages the shuttle, and once engaged, the drive actuator pulls the shuttle forward.

B. Articulated Links

Another challenge of microrobots has been to combine the high force, efficient actuators with compliant structures to create out-of-plane motion. The articulated links, which make up the leg, transfer the forces generated by the motor to the foot of the leg. One issue with planar micromachining is creating three-dimensional (3-D) structures from an inherently 2-D process. In 1992, Pister realized 3-D fold-up structures by creating pin-in-slot microhinges from polysilicon [16]. This was followed by

Manuscript received March 22, 2004; revised October 24, 2004. This work was supported in part by a NSF Graduate Research Fellowship and by DARPA/ITO SDR. Subject Editor H. Fujita.

S. Hollar was with Berkeley Sensor and Actuator, University of California, Berkeley, CA 94720 USA. He is now with Corporate Research and Development Center, Toshiba Corporation, Kawasaki, Japan (e-mail: shollar@alum.mit.edu).

A. Flynn is with the MicroPropulsion Corporation, Oakland, CA 94606 USA.

S. Bergbreiter and K. S. J. Pister are with the Berkeley Sensor and Actuator Center, University of California, Berkeley, CA 94720 USA.

Digital Object Identifier 10.1109/JMEMS.2005.850720

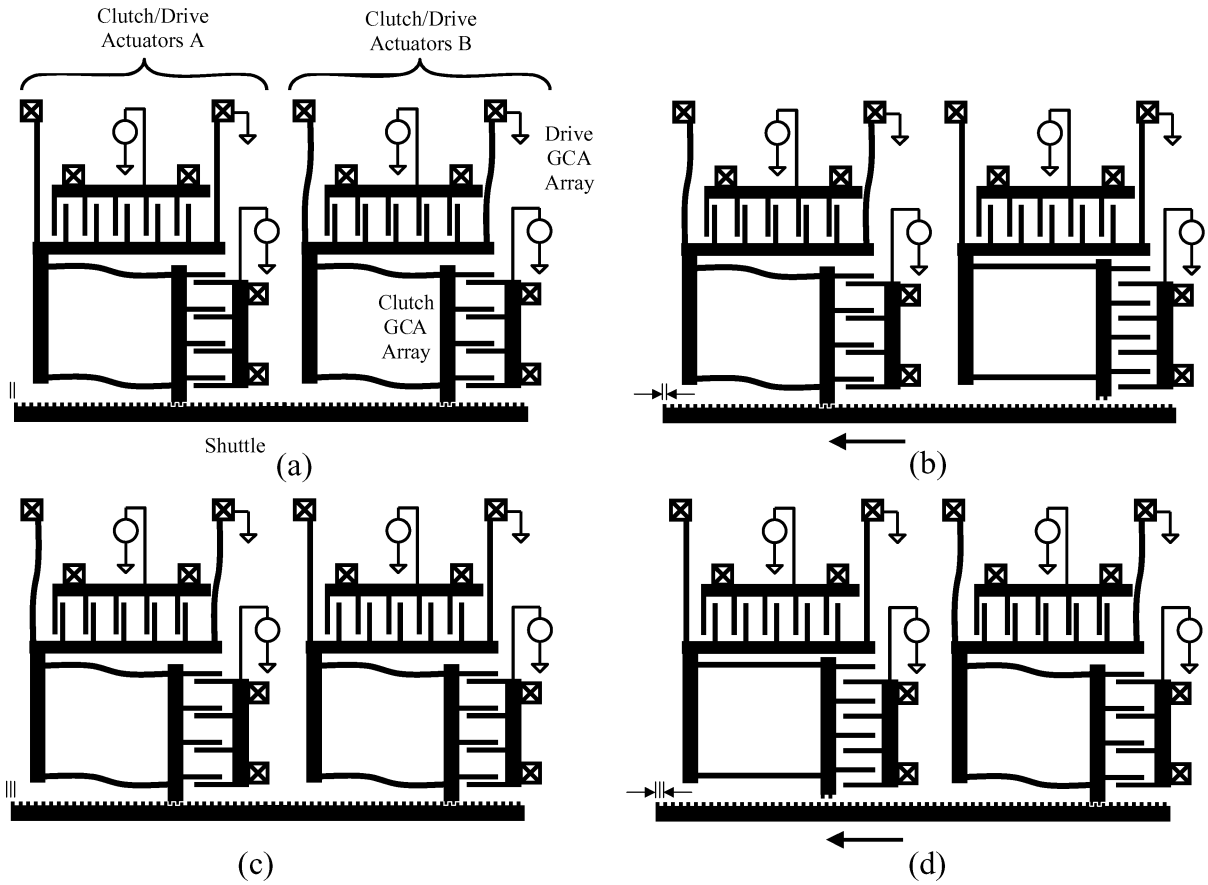

Fig. 1. Diagram of an inchworm cycle. (a) Clutch A engages shuttle. (b) Clutch B disengages shuttle and drive A pulls shuttle to the left. (c) Clutch B engages shuttle. (d) Clutch A disengages shuttle and drive B pulls shuttle to the left. Cycle is then repeated.

Suzuki who created a 3-D microrobot skeleton that could be actuated electrostatically by using polyimide flexural hinges [17]. Previous work by Yeh showed how hollow-triangular-beams (HTB) could be used to make 3-D structures from an inherently 2-D process [18]. Similar to origami, HTBs can be made by "folding" up three flat polysilicon plates. In 1999, Kladitis *et al.* built arrays of one- and two-DOF polysilicon legs. Using pin hinges, he rotated the legs 90° out-of-plane and actuated the legs thermally [19]. At that time, however, an efficient high-force motor had yet to be fabricated with compliant out-of-plane structures.

To this end, we developed a process in which electrostatic inchworm motors in thick SOI can be fabricated with thinner polysilicon structures on top. The enabling technology for this process was a novel planarization step that allowed subsequent polysilicon deposition on an SOI wafer after a silicon device layer etch [20]. This process, combined with solar cells and digital electronics, provides us with a basis for designing autonomous walking microrobots as reported in [21]. Fig. 2 shows the final product of the three-chip hybrid robot. A CMOS controller chip generates signals to drive the motors. A chip with solar cells and high voltage buffers provides power and converts the low voltage CMOS signals to the high voltage needed to drive the actuators.

In addition, this paper describes analytical methods amenable to the SOI/poly process. To improve the force density of the actuators on this robot, we present an analysis of designing at the limits of the SOI/poly process. Furthermore, utilizing this analysis, we produced designs and fabricated devices of both a one-DOF leg, which was used in [21], and a two-DOF leg. We also analyzed the reversibility of inchworm motors. In this paper, we introduce two methods by which bidirectional inchworm motion can occur.

II. Fabrication Process

We designed a new process that combines low power, high force actuators in SOI with hinged structures and linkages from traditional polysilicon micromachining. Scanning electron microscope (SEM) images of typical hinges are shown in Fig. 3(a) and (b), and a flow diagram of the five-mask process is shown in Fig. 4.

We started with an SOI wafer that had a device layer thickness of 20–50 μm [see Fig. 4(a)]. A Bosch-process advanced silicon etch (ASE) etch creates high-aspect-ratio (25:1) structures with gaps as small as 1.5 μm [see Fig. 4(b)]. This etch is used to pattern structures into the SOI device layer. Namely, gaps in the electrostatic GCAs are formed here.

It is well known that ASE etches are not perfect, having etch profiles which show lateral etching as well as tapering and footing. In our case, we focused mainly on lateral etching effects. Design rules dictating spacing accounted for any tapering that was created from the ASE etch. In addition, etch recipes

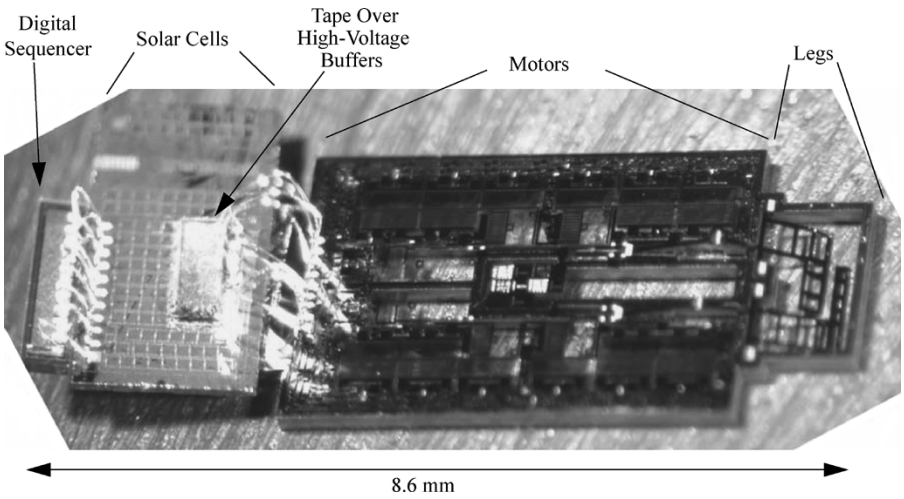

Fig. 2. Three-chip working robot. The digital sequencer outputs 3.2 V signals which are converted to 50 V on the solar-cell/high-voltage-buffer chip and sent to the robot chip to drive the electrostatic inchworm motors. The motors drive the legs via rigid links and pin-joint hinges to lift up the robot.

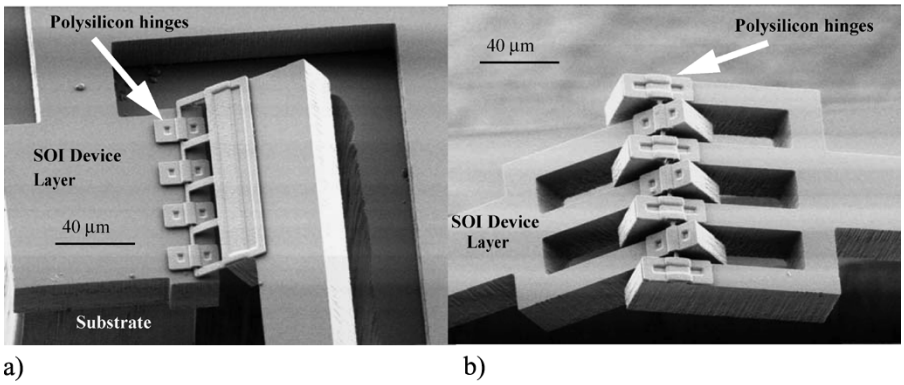

Fig. 3. (a) Polysilicon hinges attached to SOI device layer. The substrate is also seen in this SEM. (b) Interdigitated SOI device layer fingers. This hinge has a rotation range of almost 360°.

supplied by the Berkeley Fabrication staff demonstrated negligible footing effects.

However, the lateral etch effect was something we took into consideration in our designs. That is, assuming the sidewalls were etched perfectly vertically, there will still be a small but nonzero lateral etch of the trenches in the device layer. For reliable operation of the inchworm motors, we need to know the amount of lateral etch *a priori*. The ASE etch varies from process run to process run, making it difficult to design to a particular lateral etch dimension. Consequently, we adjust for this lateral etch problem by a "tweaking" step where the wafers undergo a wet oxidation step to precisely consume the silicon sidewalls down to the desired final width. This allows us to tailor the total lateral etch even though the ASEs lateral etch varies. In this case, the ASE etch and subsequent oxidation step result in a total lateral etch in the device layer of 0.5 μm.

As all trenches in the SOI device layer are up to 50-μm deep, spanning the trenches with polysilicon means filling the trenches and then planarizing before any polysilicon deposition. Most conformal coatings (i.e., low-temperature-oxide low-pressure chemical-vapor-deposition (LTO LPCVD), thermal oxide growth [22], TEOS) will not fill 50-μm-deep trenches, and certain trenches are actually large open areas, hundreds of microns wide. To solve this problem, we used the glass planarization technique developed by Yasseen.

Following [20], we spun on a glass slurry [see Fig. 4(c)], burnt out the organic [see Fig. 4(d)], and reflowed the glass at 890 °C, where the frit coalesced to form a single glass network [see Fig. 4(e)]. The wafers were fired in a low pressure furnace to minimize the occurrence of bubbles. However, we found that simply firing in low pressure did not completely remove bubbles. As a deviation from [20], we heated the glass to just below the firing temperature in an oxygen ambient at 2 torr to allow the glass to flow into deep trenches. Any remaining bubbles were then minimized during the pressurization stage from 2 to 760 torr (1 ATM).

The firing profile is shown in Fig. 5. Finally, the glass was chemically mechanically polished (CMP) to the SOI/glass interface [see Fig. 4(f)] to provide a planarized surface.

A. Bubbles and PB Contamination

For the glass planarization step, reducing bubble formation is important in designing and fabricating reliable mechanical structures. Key factors that affect bubble formation are: 1) pressure; 2) thickness of the SOI device layer; and 3) temperature. While lower pressures help eliminate bubbles in narrow trenches, more bubbles tend to form in larger more open areas.

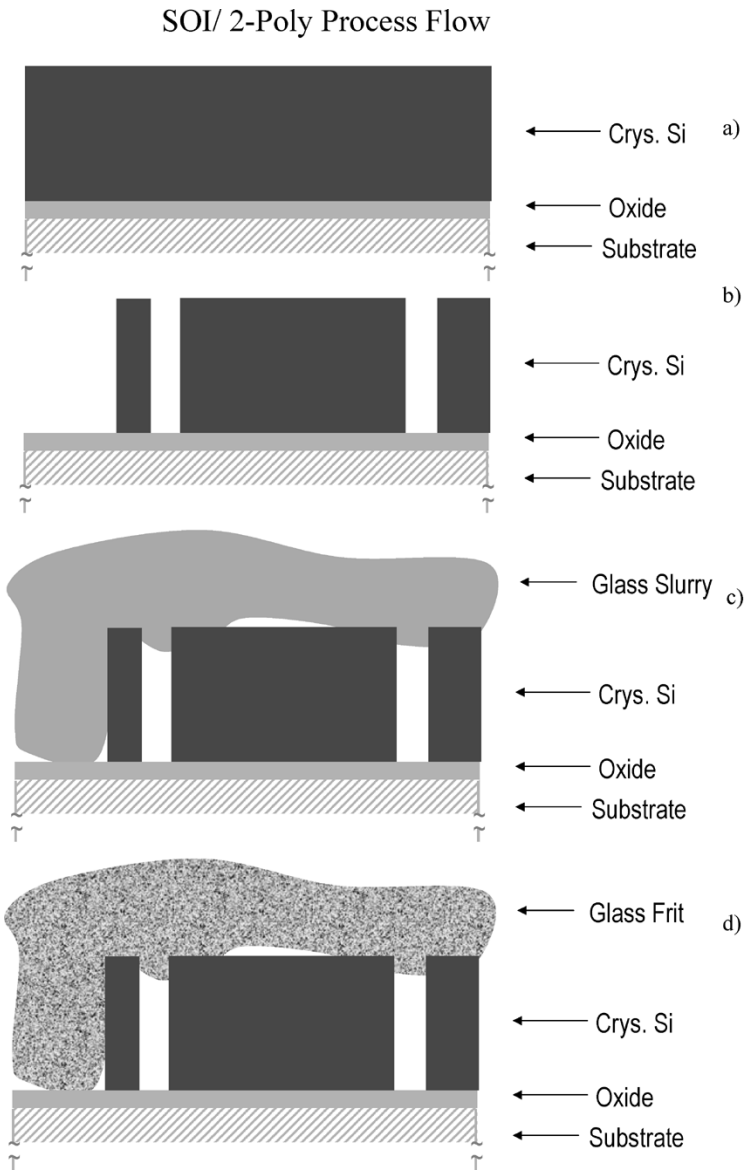

Fig. 4. Planarized SOI/two polysilicon layers process. (a) Begin with 50 μm device layer SOI wafer. (b) Bosch process ASE etch through device layer. This etch defines the actuators and legs. (c) Glass slurry made from 3-μm-glass frit and an organic transport, Alpha Terpineol, is spun on the wafer. (d) The organic transport is removed at 510 °C in an O_2 ambient.

Additionally, thicker applications of the glass frit create bubbles with larger diameters. Bubble diameters as large as the glass thickness have been observed. Last, temperature can have a significant effect. While we did most of our experiments at maximum firing temperatures of 890 °C, we noticed that firings up to 1000 °C would reduce the number and size of bubbles in the reflowed glass. In all the glass reflow experiments, some bubbles were always present after firing. Bubbles that are exposed after planarization can affect lithography and introduce unwanted polysilicon debris. However, the existing frequency and size of the bubbles are tolerable and do not significantly reduce the performance or yield of the fabricated devices.

The glass frit, itself, is one of Ferro Corporation's passivation glasses. IP900-VWG has a very low alkali metal content (>50 ppm) and is composed of 50% SiO_2, 30% PbO,12% B_2O_3, and 8% Al_2O_3 by weight. One might be concerned that Pb could easily contaminate the quartz LPCVD tubes during silicon and oxide depositions. However, unlike the piezoelectric material lead zirconate titanate (PZT), whose high Pb diffusivity at low temperatures is based on dislocations in the crystal lattice, IP900-VWG is an amorphous structure whose Pb atoms are surrounded by an average of six Si atoms. Pb diffusion does not become appreciable below the softening point, 771°C. To demonstrate this point, we performed secondary ion mass spectroscopy (SIMS) analysis on the Si-Pb glass to determine the Pb content.

Fig. 6 shows the concentration of Pb at the interface of the deposited low-temperature-oxide (LTO) and the glass. Wafers were tested at two stages in the SOI/poly process, once during a polysilicon deposition and another at 900 °C during the anneal. For the former, Pb diffused less than 50 nm into unannealed LTO after 10 h at 610 °C due to the fact that the glass was below its softening point and the atoms in the glassy network remained essentially immobile. After 1 h at 900 °C, Pb only diffused

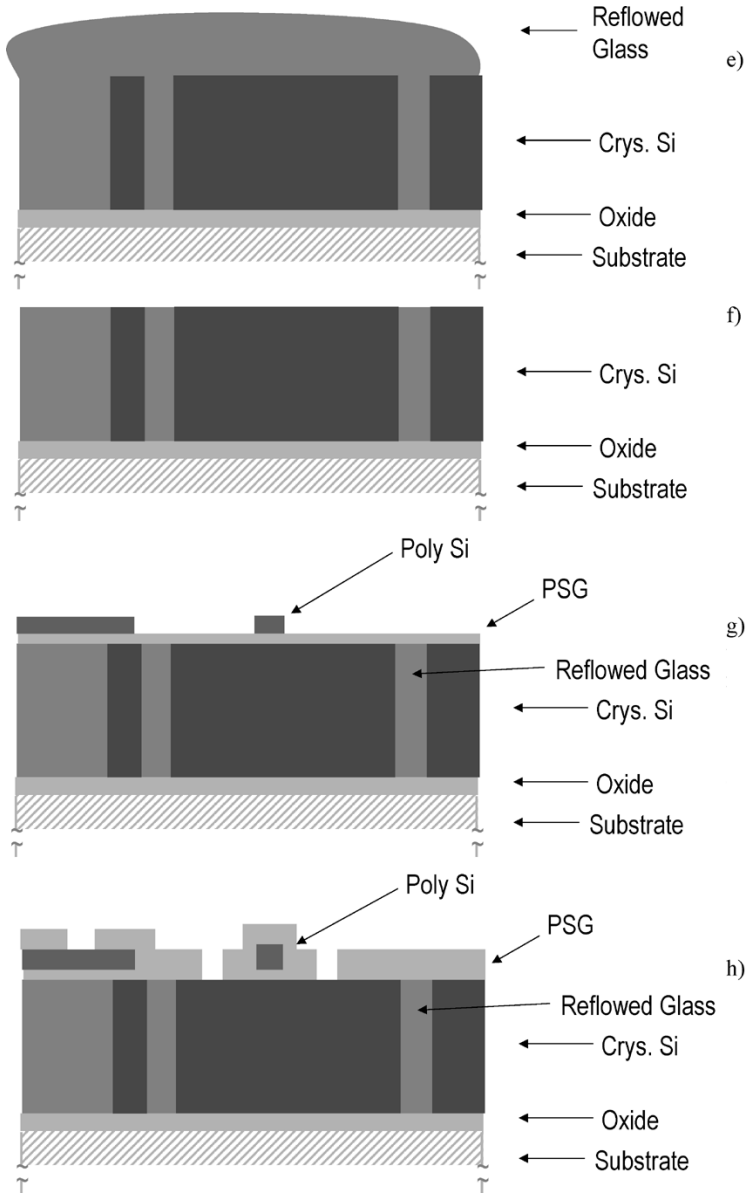

Fig. 4. *(Continued.)* (e) The glass frit is then reflowed at 890 °C to form a single glass network. Bubbles are reduced by doing a combination vacuum/atmospheric glass firing. (f) A KOH-based slurry is then used to planarize the wafer. Often a single layer of glass slurry only adds $\sim 25\ \mu\mathrm{m}$ of glass. For thick device layers, steps (c) through (e) should be repeated. (g) After planarization, the wafer can be surface micromachined. A 0.5-μm-PSG layer is initially deposited followed by 2.5 μm of undoped poly-Si. The poly-Si layer is then patterned using DRIE. (h) A 1.5-μm layer of PSG is then deposited. Careful calculation of layer thickness was performed to allow pin hinges to rotate freely in their pockets. The first and only contact etch is then performed.

approximately 400 nm. Depositing LTO over the glass before further processing ensured negligible out-diffusion of Pb in subsequent steps.

B. Micromachining

After planarization, wafers underwent standard polysilicon micromachining. Three masks were used to define two structural polysilicon layers (fine-line lithography: 2 μm). 0.6 μm of phospho-silicate-glass (PSG) was first deposited on the planarized SOI surface, followed by a 2-μm-thick layer of patterned polysilicon. After another 0.6 μm PSG deposition, the wafer was patterned with a contact mask used for anchoring the following polysilicon layer. Next, 2 μm of the second and final polysilicon layer was deposited.

Because our focus was designing mobile microrobots, we tried to reduce the weight of the robot by removing any unwanted silicon. We performed a grind and polish on the backside from a total wafer thickness of 525 μm down to 300 μm. Afterwards, a backside substrate etch was performed using the same Bosch ASE process as before [see Fig. 4(g)–(j)]. Due to the wafer thickness and stress from the glass and the additional polysilicon micromachining, the wafer had a radius of curvature of approximately one meter.

For the release, a solution of HCl, HF and $\mathrm{H_2O}$ was used in a timed etch on the planarized glass, buried thermal oxide, and PSG. The goal was to etch long enough to remove the PSG and reflowed glass, but not so long as to remove all of the buried oxide. The reflowed glass etches approximately 30 times faster

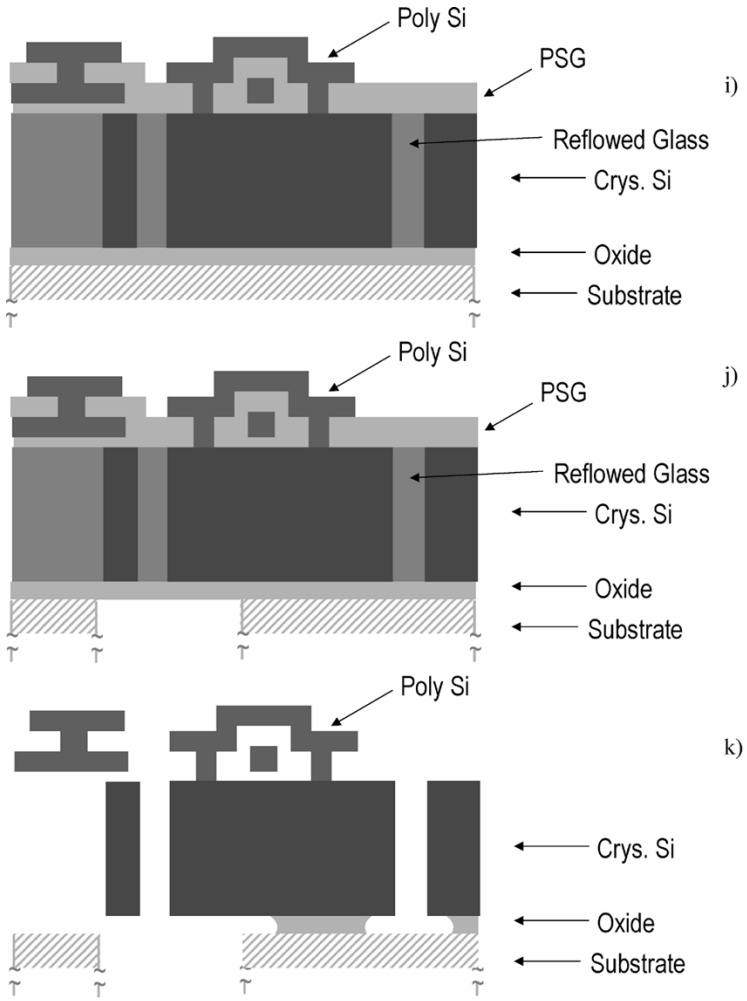

Fig. 4. *(Continued.)* (i) A 1.5-μm layer of undoped poly-Si is deposited and patterned. The wafer is then annealed at 900 $\circ$C for 1 h to dope the poly-Si from the PSG. (j) The wafer is then backside ground to 300 μm total thickness. A backside etch completes the process. Backside exposure helps reduce the total weight of the robot. Additionally, debris and stiction issues are also reduced in the areas where the backside is removed. (k) The backside also defines scribing lanes. The wafer is then broken up into chips and individual chips are released. A timed $HF/HCl/H_2O$ etch removes the glass. A final HF timed etch selectively removes the buried oxide.

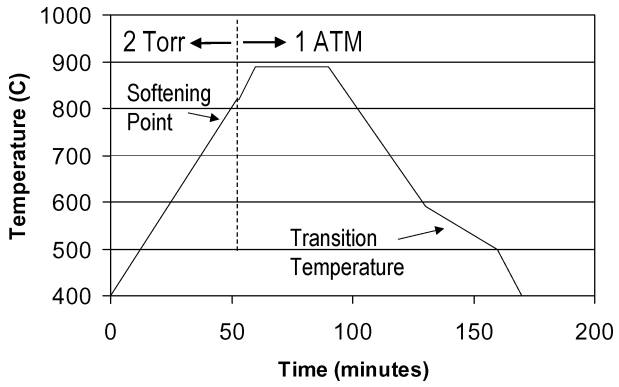

Fig. 5. Firing profile of glass. The glass was heated in an oxygen ambient at 2 torr to allow the glass to flow into deep trenches. Any remaining bubbles were then minimized during the pressurization stage from 2 torr to 1 ATM.

than the buried oxide, so tight tolerances in the undercut of the thermal oxide were maintained. Narrow SOI blocks were fully undercut while wide SOI blocks were still anchored to the substrate via the thermal oxide [see Fig. 4(k)].

An unfortunate by-product of the release was that alumina particles were scattered across the wafer. Since the glass frit was created at Ferro Corporation using an alumina ball mill for an extended period of time, alumina flakes on the order of 0.5 μm were present in the glass mixture. To remove the alumina particles, the devices were placed in a heated bath (50 °C) of NH_4OH, H_2O_2, and H_2O. Critical point drying was performed to avoid damage from water surface tension.

The release of the chips was not a straight forward endeavor. Initial releases had very low yield on the order of 20%. We encountered two major issues during the release step: 1) particulate contamination and 2) broken polysilicon structures. When we released robots polysilicon side up, a large number of particulates were found in the trenches. In addition to being mechanical barriers, these particulates electrically shorted actuators to ground. Since GCAs operate with no dc current, a key metric to determine the cleanliness of the release was based on the *I–V* curve of the electrostatic actuator. If no contaminants shorted out devices, experiments showed that the actuators would operate at less than 1 nA of current for voltages exceeding 50 V.

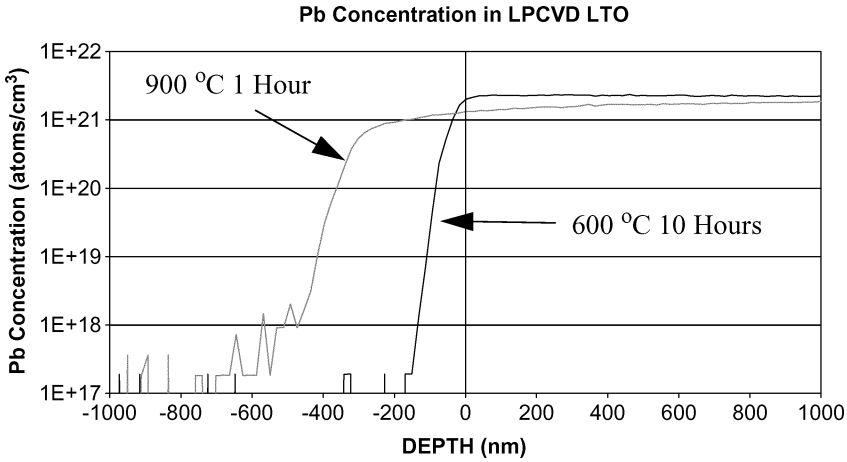

Fig. 6. Lead diffusion into LPCVD LTO. SIMS was used to determine the concentration of lead in LTO and the glass.

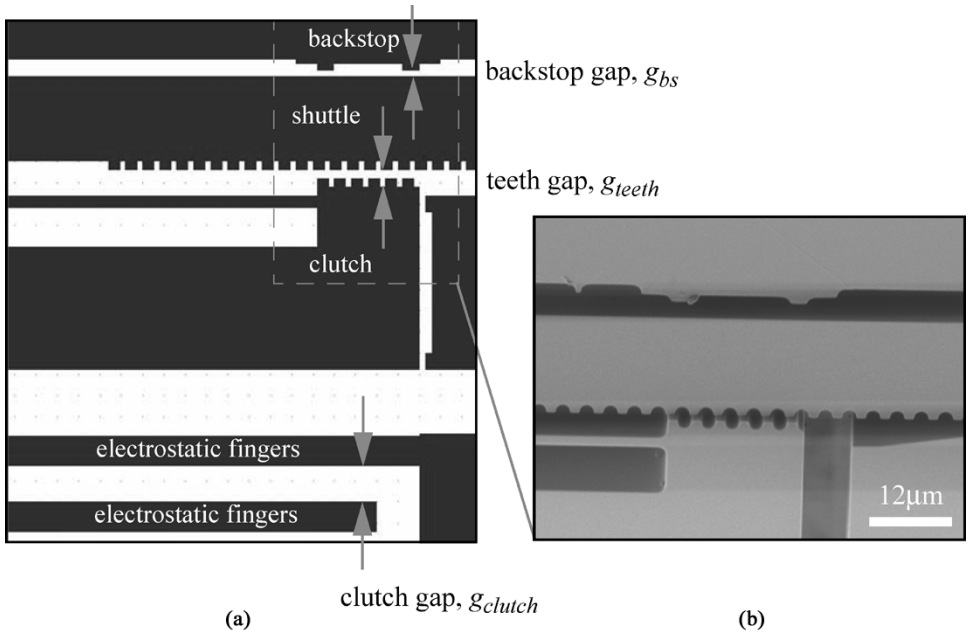

Fig. 7. (a) Layout of backstop, shuttle, and clutch. Spacing of the gap between the shuttle and backstop g_{bs} and between the clutch and shuttle g_{teeth} dictate the minimum spacing between the GCA fingers g_{clutch}. (b) SEM of actual backstop, shuttle, and clutch.

Some initial releases, however, showed leakage currents up to 20 mA.

Using Seiko's 8800 FIB System with energy dispersive x-ray analysis, we identified the chemical make-up of some of the particulates. We identified particles composed of aluminum, phosphorus, calcium, and silicon. It was unclear where the particulates came from, though. One possibility was from the release setup and critical-point dry, and another possibility was when the glass was first fired. We found that rigorous cleaning of the dishes used in the release and developing a disciplined attitude toward release protocol were mandatory to achieve cleanliness. Performing the release with the chips upside-down, furthermore, dramatically decreased the number of particulates. Electrical tests verified the cleanliness with less than 1 nA leakage currents at 50 V. Last, agitation during the glass solution etch further removed particles. Using all of these methods, our yield during the release eventually improved to 50%.

III. Improving Force Density

A. Process Considerations

In the SOI/poly process, a high-aspect-ratio advanced silicon etch (ASE) defined the inchworm motors in the SOI device layer. For high force density electrostatic actuators, it was desirable to have the smallest gaps and thickest device layer possible. The thickness of the SOI device layer could be optimized based on the minimum resolution of the lithography and the aspect ratio of the ASE etch. Our lithography allowed us to conveniently draw 2 μm lines, and the ASE etch gave us an aspect ratio of 25:1.

A significant factor affecting the maximum electrostatic force density for a given process is the lateral etch. Thus, the deeper the etch, the wider the sidewalls would be. For device layers that were too thick, lateral etch effects could significantly reduce the electrostatic force which decreases as the square of the distance

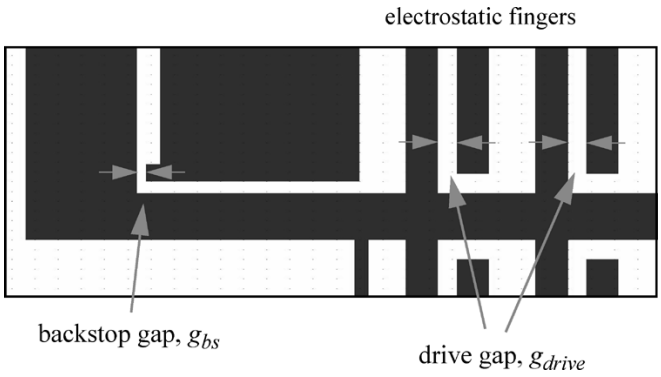

Fig. 8. Layout of drive and drive backstop. Spacing of the gap between the backstop and drive frame, g_{bs}, dictates the minimum spacing between the GCA drive fingers g_{drive}.

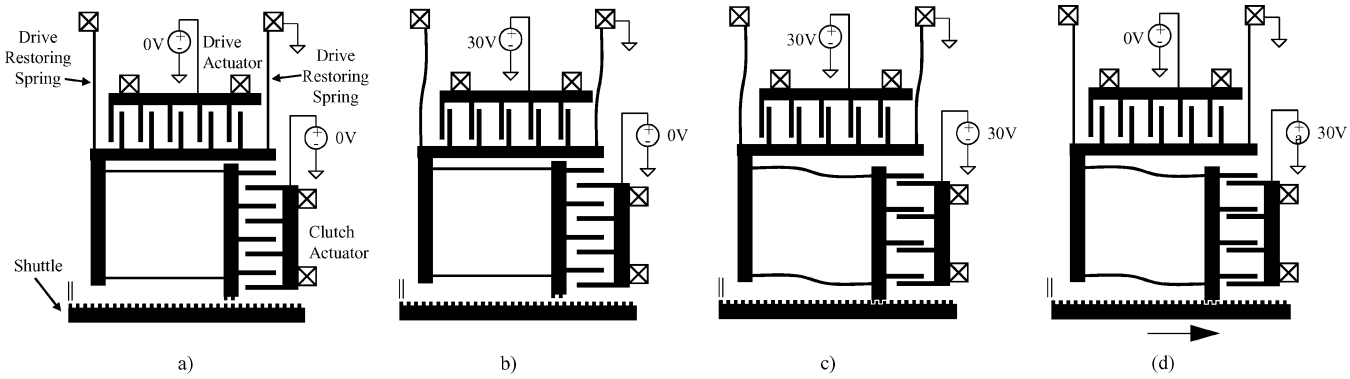

Fig. 9. Drive restoring spring. a) In the initial position both the clutch and drive actuators are at rest. b) The drive actuator is initially preset before the clutch engages. c) Clutch engages while drive is present. (d) Turning off the drive actuator allows the drive restoring spring to pull the shuttle backward.

of the gap. On the other hand, for device layers that were too thin, the force would be limited by the actuation area which depends linearly on the depth of the trench. Therefore, for maximum force density, the lateral etch would have to be on the order of the minimum line width of the process. If we assume the aspect ratio is mostly due to the lateral etch, this gives us a guideline for the selection of the wafer thickness. Here, we chose 50 μm to have the lateral etch approximately equal to the minimum line width.

Furthermore, the lateral etch affects backstop spacings, electrostatic gaps, and tooth widths in the inchworm motors. If the lateral etch can be predicted *a priori*, the design of the inchworm can be modified to account for this irregularity. In the next section, we discuss the effect lateral etching has on the inchworm motors.

B. Gap Spacing

Fig. 7(a) shows the Cadence layout of the clutch, shuttle, and backstop of an inchworm motor. Two clutch fingers are also shown toward the bottom of the figure. The drawn gaps of the backstop, teeth, and clutch are $\mathrm{g_{bs}}$, $\mathrm{g_{teeth}}$, and $\mathrm{g_{clutch}}$, respectively. Fig. 7(b) shows a close-up SEM image of the fabricated clutch and shuttle. It is important to remember that if a lateral etch uniformly etches the perimeter of the structures with a width of δ, the final gap spacing is an additional 2δ on top of the originally drawn gap width. To prevent shorting of the electrostatic fingers, the gap between the clutch GCA fingers must be larger with a sufficient margin than the sum total of the backstop gap and teeth gap.

This requirement is expressed by

$$(2\delta + g_{bs}) + (2\delta + g_{\mathrm{teeth}}) < 2\delta + g_{\mathrm{clutch}} \tag{1}$$

after simplification the inequality yields

$$2\delta + g_{bs} + g_{\mathrm{teeth}} < g_{\mathrm{clutch}}. \tag{2}$$

Here, we see that as the lateral etch increases, $\mathrm{g_{clutch}}$ must also increase to prevent finger shorting. In the SOI/poly process, we tailored the undercut so that $\delta = 0.5$ μm. With $g_{bs} = 1.5\,\mu$m, and $g_{\mathrm{teeth}} = 4\,\mu$m, g_{clutch} must be greater than 6.5 μm. In this case we made g_{clutch} 8.5 μm giving us a tolerance of 2 μm.

Similar arguments follow for the drive actuator. In this case, there are only two gaps of interest. As Fig. 8 shows, the final drive gap must be greater than the final backstop gap. Again with a lateral overetch of δ, we extract the following

$$2\delta + g_{bs} < 2\delta + g_{\mathrm{drive}} \tag{3}$$

and simplifying we have

$$g_{bs} < g_{\mathrm{drive}}. \tag{4}$$

The lateral etch on both gaps cancels out the effect. For our motors, $g_{bs} = 2.0$ μm for the drive back-stop and $g_{\mathrm{drive}} = 4\,\mu$m. Again, this gives a tolerance of 2 μm.

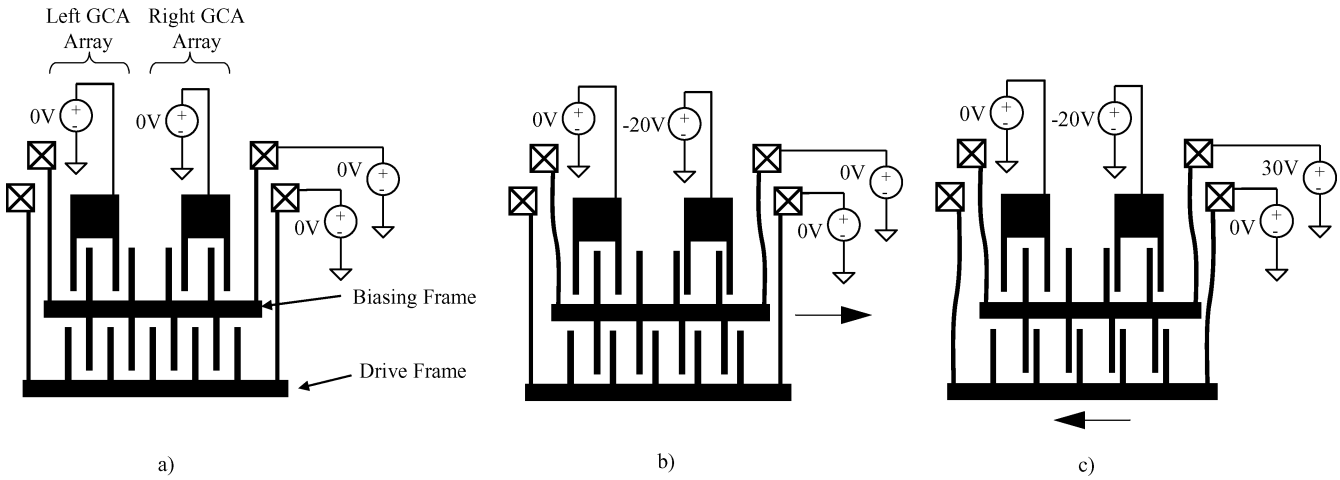

Fig. 10. Biasing GCA array. a) The diagram shows the right/left GCA arrays and the drive GCA array. Clutch GCA array not shown. b) To move to the left, the biasing frame is first actuated to the right by applying a -20 V signal to the right GCA array. Gap stops not shown. c) To move the drive frame to the left, a 30 V signal is then applied to the drive GCA array.

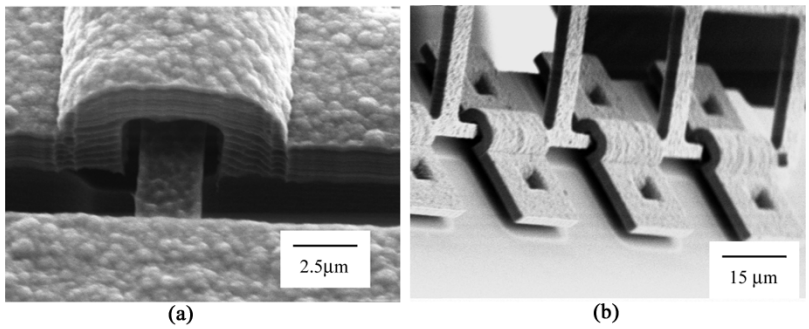

Fig. 11. SEM images on pin. (a) Image of hinge. The striations on the POLY2 layer are artifacts of the ASE etch. (b) Image of a rotated hinge.

For both the clutch and drive actuators, the effect of lateral etch also reduces the initial force the GCAs can produce. The inchworm's initial force comes from the drive actuators in their "normally open position," the point where the gap distance is largest. This is determined by

$$g_f = 2\delta + g_{\text{drive}}. \tag{5}$$

Based on (1) and (3), the actual gap width, g_f, is 5 μm instead of the drawn gap of 4 μm. This represents a 36% difference between the calculated force based on the drawn gap and the actual gap.

The force applied on the shuttle by the clutch is determined by the gap spacing of the clutch GCA array after the clutch has engaged. With a sufficient clutch force, the clutch will have pushed the shuttle fully against the backstops. In this case, the final electrostatic gap spacing is 2 μm which produces a force on the shuttle approximately 20$\times$ larger than the clutch's normally open position. With such a large increase in engagement force, the clutch GCAs can be designed to be substantially smaller than the drive GCAs of the inchworm actuators.

IV. Bidirectional Inchworm Actuation

A. Method 1

One method to reverse the motion of the shuttle is to reverse the control sequence of the inchworm motor. Fig. 9 shows just a single clutch/drive actuator pair, but this is sufficient to demonstrate the reversal mechanism. In the initial position, both the clutch and drive actuators are at rest [Fig. 9(a)]. The drive actuator is initially preset before the clutch engages [Fig. 9(b)]. Once the clutch engages, the drive is already preset so that the clutch engages the shuttle one half-pitch in the reverse direction [Fig. 9(c)]. Last, the electrostatic drive force is turned off allowing the restoring spring to force the shuttle in the reverse direction [Fig. 9(d)].

The restoring force depends on the drive restoring spring (see Fig. 9(a)). In the static view, the force of the spring should be greater than the load through at least half the period of motion, which is half the tooth pitch. Furthermore, total displacement during actuation is larger than half a period of motion due to the etch in the lateral direction. Based on these considerations, the restoring force can be calculated [23].

The 2-DOF leg presented later is driven using this reversible mechanism. The drive restoring spring constant is 5.4 mN/mm, and the drive restoring spring needs to maintain a load up to 0.5 μm of deflection. Therefore, the shuttle load in the reverse direction is limited to 5.4 μN.

B. Method 2

A different inchworm design that has a fractional effect on force density yet offers equivalent output force in both directions is shown in Fig. 10. The addition of two small sets of GCA

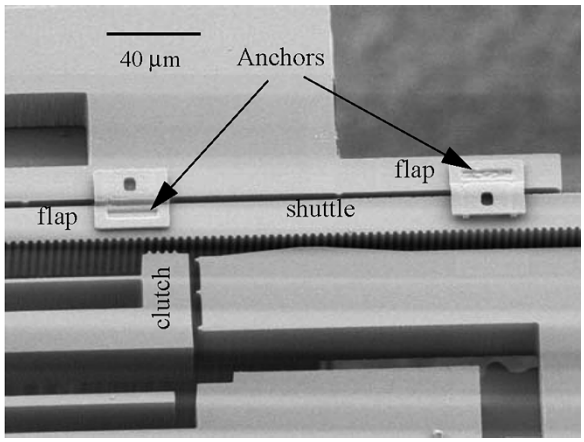

Fig. 12. The inchworm motor shuttle and pawl. The flaps are used to constrain the motion of the shuttle. Flap anchors are labeled to show the direction of the flap constraint.

arrays (left and right) enables one to bias the drive array for forward or reverse actuation. Fig. 10(a) shows a cut out section of the motor that contains the drive array and biasing array. The clutch mechanics are identical to the original motor and therefore, are not included in this figure. The biasing frame is used to bias the drive GCA array in one direction or the other.

In Fig. 10(b), the right GCA array is charged to −20 V, causing the biasing frame to actuate to the right. This places the drive electrodes closer to one set of the electrostatic fingers than the other. Gap stops (not shown) prevent the left/right GCA arrays from shorting. In Fig. 10(c), the drive frame is actuated forward by applying 30 V onto the biasing frame.

The biasing frame is held against an SOI anchor by the gap stops preventing it from further moving to the right. Actuation of the drive frame to the left creates an opposite force to the right on the biasing frame. The counterbalancing force on the biasing frame comes from contact with the gapstops and not from the biasing GCA arrays. Therefore, the biasing GCA array need not produce a large force, only just enough force to initially move the biasing frame. Consequently, the biasing GCA array need only be a fraction the size of the drive GCA array and therefore the force density of the actuator is not significantly degraded.

This motor design is complicated by the addition of two more signals and thus requires a more complex signal stream to drive the motors. If negative voltages are available, the biasing electrodes can be simply biased before a right or left motion commences. Then, the signal streams for the drive and clutch actuators can remain the same. If negative voltages are not available, the motors must be driven by switching all six signals during the inchworm cycle. For a unidirectional inchworm motor, only 4 steps are needed in a single cycle, but for the bidirectional motor, we used 8 steps for a single cycle.

V. Additional Design Guidelines in SOI/Poly Process

Using the SOI/poly process, we designed an 8 mm × 3 mm robot structure that uses inchworm motors and hinged SOI legs. We used pin hinges [Fig. 11(a) and (b)] in a one-DOF leg whose

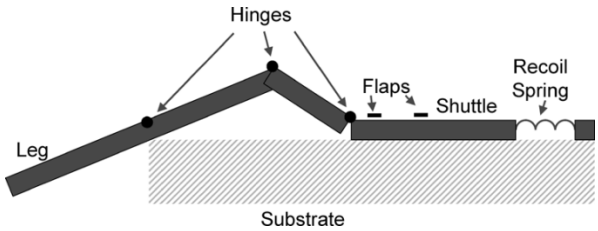

(a)

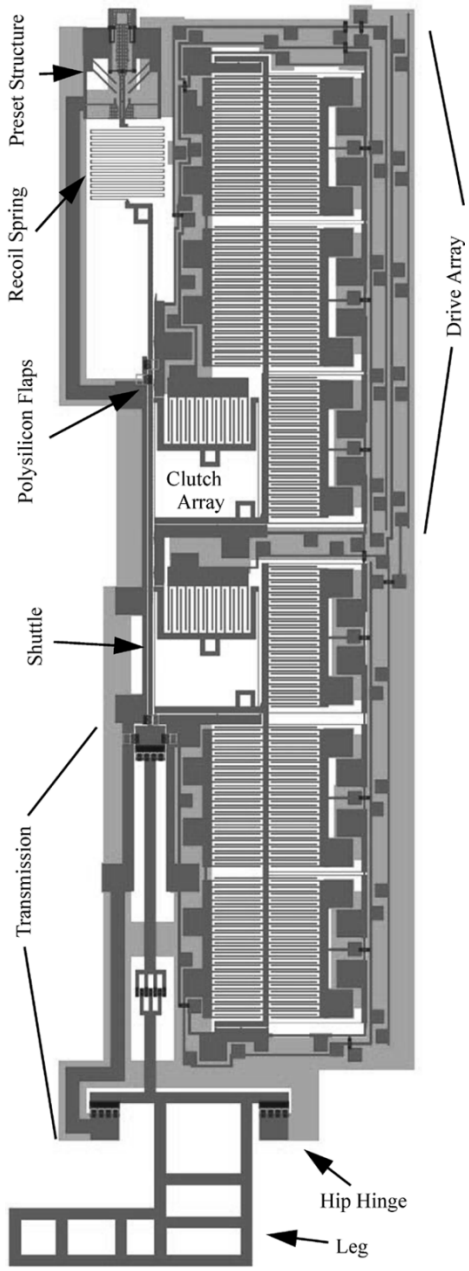

(b)

Fig. 13. (a) Schematic of one-DOF leg. The one-DOF leg is composed of three rigid links and three hinges. These form the base of the linkage, transforming the displacement from the shuttle to leg motion in front. Since the inchworm drives predominately in one direction, a recoil spring is used to reset the leg motion upon completion. (b) CAD drawing of single leg and inchworm motor of the robot. The leg/motor length is 6 mm.

linkages are depicted in the kinematically equivalent 2-D diagram in Fig. 13. The robot design incorporates a number of

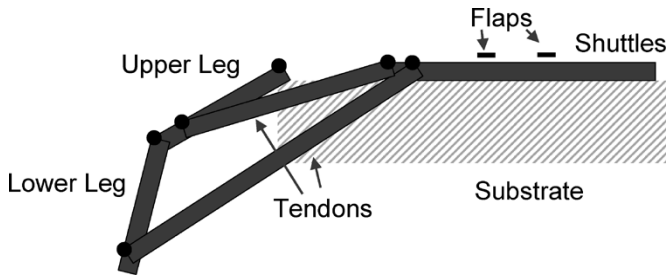

Fig. 14. Two-DOF leg schematic. Two motors drive the tendons of the upper and lower legs. Flaps, again, constrain the motion of the shuttles. However, the shuttles have no recoil spring, so they reverse direction by reversing the driving sequence of the inchworms.

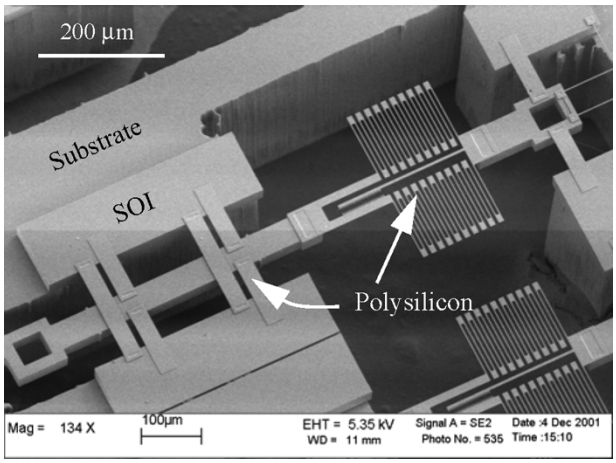

Fig. 15. SEM of the sliding test structure. A vernier spring was used to measure the force required to move polysilicon flaps over the SOI device layer.

design advantages from the process and remedies some problems associated with Yeh's original inchworm motor [24].

Since both the SOI and polysilicon layers act as conductors, the motor wiring is not constrained to any particular layer. This allowed us to draw connections from the motors to a set of bond pads in the back of the robot. However, wiring over long distances was problematic since both the SOI and polysilicon are susceptible to pull-in after the PSG and thermal oxide layers are removed. To alleviate this problem, SOI anchors were placed periodically along the wire. These anchors provided enough mechanical stiffness to withstand electrostatic forces between the SOI wiring and the robot substrate.

The improved inchworm motors also utilized flaps to constrain the motion of the shuttle to the plane of the device. As seen in Fig. 12, the flap attached to the shuttle on the left prevents the shuttle from falling through the wafer, and the flap over the shuttle on the right prevents the shuttle from popping up out-of-plane. With the inclusion of flaps, the shuttle no longer needs to be constrained by parallel flexures as in [24]. To reduce surface contact between the flaps, dimples are formed using the first polysilicon layer as a sacrificial place holder.

Preset structures can be set so as to maximize mechanical advantage during the initial actuation. Without preset structures, the out-of-plane moment arm is limited to the thickness of the SOI device layer. As seen in Fig. 18, a preset structure can be translated and latched into place with a manual probe. Guided by the preset structure, the shuttle is also repositioned.

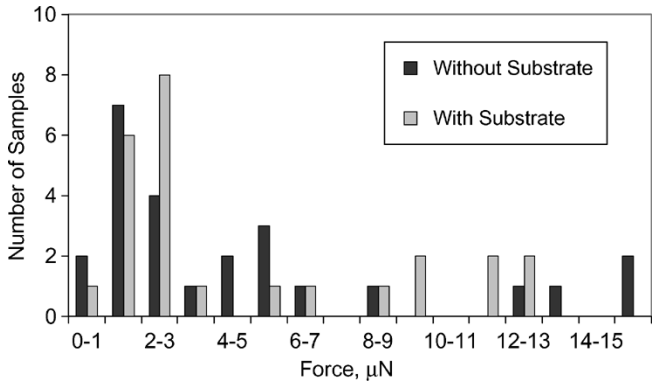

Fig. 16. Force measurements taken from the sliding friction test structures. A mean force of 4.6 μN and median of 2.5 μN were the same for sliders with and without a substrate.

VI. One-DOF Robot Leg Design

In previous sections, we discussed basic mechanical components for out-of-plane actuation and design considerations for inchworm motors. Here, we use those components to design an inchworm-actuated, out-of-plane, one-DOF leg. Fig. 13(a) shows the conceptual design of the leg. The leg is based on a slider-crank mechanical construct. A combination of sliders and hinges transform linear displacement into angular rotation.

Designing the lengths of the leg segments appropriately, we can get a 1:1 mechanical coupling from shuttle actuation to vertical leg distance. Based on the relationship between robot weight and motor force, we optimized for the required size of the inchworm motors. In this case, we calculated an inch-worm motor area of 7.5 mm^2.

Given these constraints, we designed a leg and inchworm motor structure shown in the CAD lay-out in Fig. 13(b). The majority of the backside is removed to reduce the total mass of the robot. Furthermore, substrate is removed underneath the SOI device layer areas that contain moving structures, such as the shuttle and the moving frames of the inchworm. This reduces the chance these structures will stick to the substrate after the release of the structures from the glass.

To reset the leg, a serpentine spring allows the shuttle to recoil to its nominal position after the leg is actuated forward. The spring is designed with a very low spring constant so as not to adversely affect the forward force of the motors. The preset structure located near the back of the robot presets the shuttle 150 μm for an initial moment arm. This sets the shorter leg 30° out of the plane. Last, a set of four hinges converts the linear motion to angular motion. Two "hip" hinges are placed on either side of the leg. This helps reduce excessive moments on the hinges from leg tip forces that could occur off-axis from the shuttle. Flaps with dimples are also used to constrain the motion of the shuttle to lie within the plane of the inchworm.

Finally, to protect the legs during release and assembly, a rollbar surrounds the legs (see [21, layout figure]). The rollbar, consisting of substrate and device layer SOI, is substantially more robust than the legs with polysilicon hinges. The legs are held in place by polysilicon tethers that attach the legs to the rollbar. Robots that are dropped or bounced around during the

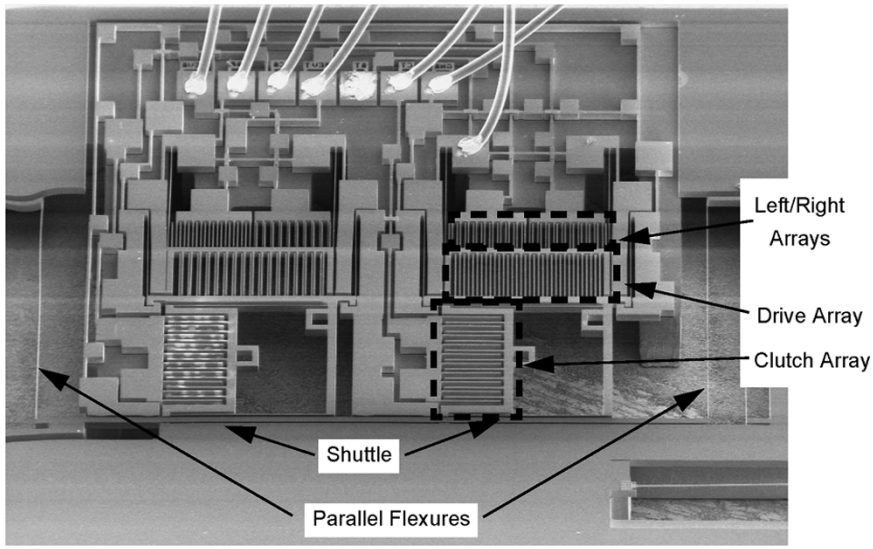

Fig. 17. Bidirectional motor. The left/right GCA arrays slightly bias the drive frame one way or the other to cause the drive actuator to go forward or backward.

release can absorb hits on the rollbar much more effectively than on the legs [shown in two-DOF leg, [Fig. 13(b)].

VII. Two-DOF Robot Leg

While two one-DOF legs were used in the solar-powered robot [21], one can easily imagine designing more complex linkages through the SOI/poly process for future robot designs. To this end, we have designed an inchworm actuated two-DOF leg (see Fig. 14 for the conceptual drawing). The leg uses two inchworm motors to drive two shuttles. Each shuttle is attached to a tendon which in turn moves an upper or lower leg. The upper leg assembly is a slider-crank mechanical construct, and its orientation depends only on one of the shuttles. The lower leg is part of a 5-bar crank-slider construct, and its orientation depends on the positions of both shuttles.

A diagram of the leg is shown in Fig. 14. Polysilicon flaps constrain the motion of the shuttle to remain in the motor's plane. A rollbar [shown in Fig. 20(a)] is used to tether the legs in place and protect the legs during release and assembly. For future designs, as more degrees of freedom are implemented, crossover beams will be needed to bridge overlapping mechanical structures. In this case, only one poly-silicon cross-over beam is used. The polysilicon cross-over beam [shown in Fig. 20(b)] bridges the lower leg structure overtop one of the tendons.

One way we simplified the mechanical design of the two-DOF leg over the one-DOF leg is the removal of the recoil spring. In this case, the shuttle is suspended only by the polysilicon flaps. Lifting the leg requires only enough force to overcome the friction of the flaps and hinges. This frictional force should be small compared to lifting a robot's weight. Since we require large forces in one direction and small forces in the other, we can simply reverse the driving sequence of the inchworms to lift the leg (bidirectional motor method 1). This is a good example of how we can reduce the complexity of the mechanical design by marginally increasing the complexity of the sequencing.

VIII. Experimental Results

A. Surface Friction

By adding polysilicon flaps to constrain the motor shuttle, we introduced a possible source of adhesion and friction to the motor design. Yeh demonstrated in friction tests of polysilicon on nitride that the force required to slide a shuttle along the substrate and rotate an unloaded hinge required between 1–43 μN, values much greater than the force due to the weight of the lever arm (3.2 nN) [25].

Our aim was to measure frictional forces that an inchworm actuator must overcome to move the shuttle. To do this, we designed simple SOI sliding test structures attached to polysilicon vernier springs (Fig. 15). The test structures were designed both with and without substrate underneath. This allowed us to compare sliding polysilicon flaps along SOI to sliding an SOI beam along the silicon substrate.

A histogram of the force required to overcome static friction and adhesion in each of the test structures is shown in Fig. 16. Force required to move the SOI beam ranged from 0.5–13 μN with substrate and 0.5–15 μN without substrate. Peak value recurrence for both sliding structures was between 1–3 μN.

It is important to note that the tests were performed shortly after the structural release. After storing the test structures in normal laboratory conditions for approximately one month, sliders with polysilicon flaps required forces much greater than the vernier springs could measure ($\gg 25\ \mu$N). This was probably due to adhesive forces from ambient moisture and will likely need to be addressed in future robot design and testing.

B. Bidirectional Motor

Motors were actuated using a programmable Atmel AVR microcontroller whose I/O pins interfaced to an Analog Devices AD8600 16 Channel DAC. Amplifiers on the channels converted the 5 V maximum outputs of the DAC to a maximum possible 160 V output. The inchworms were limited to 65 V, however, because of electrostatic pull-in of the GCA fingers.

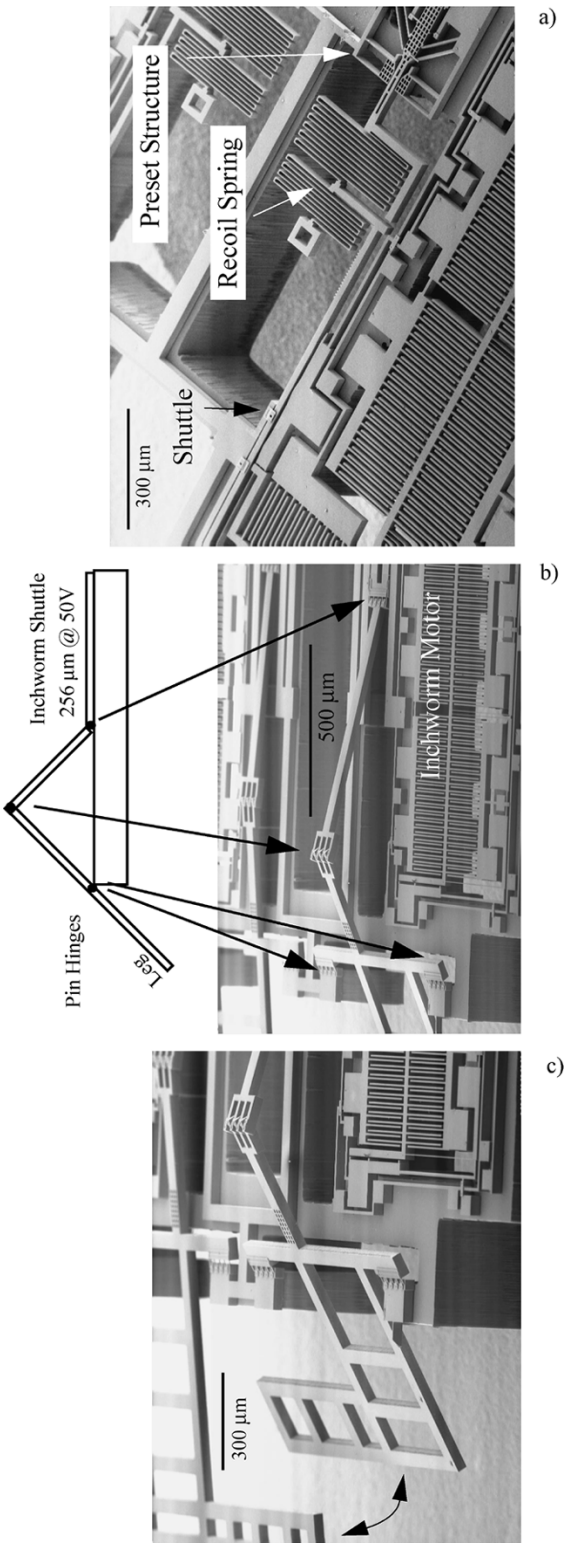

Fig. 18. (a) SEM: Shuttle, recoil spring, and preset structures. These structures are located near the back of the inchworm motors. (b) Kinematic diagram of robot leg and SEM of linkage structure. Arrows are used to show the position of hinges relative to the diagram. (c) SEM of robot leg in preset condition. Leg was actuated through almost 30° of angular deflection.

The programmability of the test setup allowed us to troubleshoot the inchworm motors and characterize the speed of individual

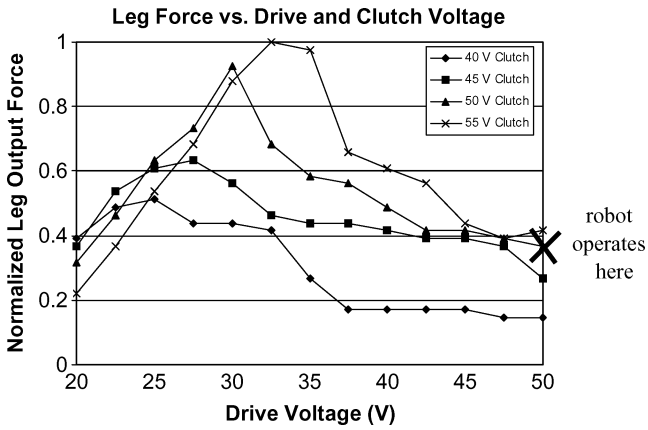

Fig. 19. Relative force versus clutch and drive voltages for long leg.

steps of the inchworms. In the microrobot, we designed the inchworm motors to be run from solar cells where the solar cell array voltages ranged from 30 to 50 V. Thus, the voltages we selected in our experiments were typically in this range.

Here, we designed and tested a bidirectional inchworm motor (see Fig. 17). Because this design was a test structure, the shuttle is suspended by a set of parallel flexures rather than driving a leg. The motor was fabricated in an area $1.9 \times 1.6\ \mathrm{mm}^2$ and demonstrated both right and left motions at speeds up to 5.5 mm/s with a total travel of 224 μm in each direction. The inchworm motor was driven with a 40 V drive and clutch actuation voltage, and to achieve pull-in during the biasing phase, the right/left actuation voltage was set at 20 V. With a spring constant of 0.02 $\mu\mathrm{N}/\mu\mathrm{m}$, the maximum load on the motor was not more than 2.25 μN.

C. One-DOF Leg

Finally, we tested the robot motors and legs. This device consisted of the robot frame, motors, and two one-DOF legs. SEM images of the fabricated SOI/poly chip can be seen in Fig. 18(a)–(c). Each motor we tested measured $700\ \mu\mathrm{m} \times 4\ \mathrm{mm}$. The motor was calculated to maintain a force of at least 400 μN at 50 V. Before testing the legs, we preset the shuttle by 150 μm using the latch structure in Fig. 18(a). This gave the leg an initial starting angle of 34° relative to the plane of the motor [Fig. 18(c)].

We demonstrated both legs working at shuttle speeds of 4 mm/s, over 100 times, with no failure (for videos, see [26]). Each leg swept through 30° of motion yielding an angular rotation rate of $480^\circ/\mathrm{s}$. Force measurements were also taken from a vernier spring gage from MEMS Precision Instruments [27]. Based on the actuated displacement of the spring, we back-calculated the force exerted at the tip of the leg. Force measurements have shown that the long leg produced from 30 to 60 μN of force when the drive and clutch voltages of the inchworm motors were 32 and 50 V, respectively. The wide measurement range may be due to the low spring constant of the gage ($0.15\ \mu\mathrm{N}/\mu\mathrm{m}$) which caused the leg to jam on the vernier spring over wide sweeps.

Nevertheless, we were able to map out a relative force space of the long leg for given drive and clutch actuation voltages (Fig. 19). The force increases for increasing drive voltages up

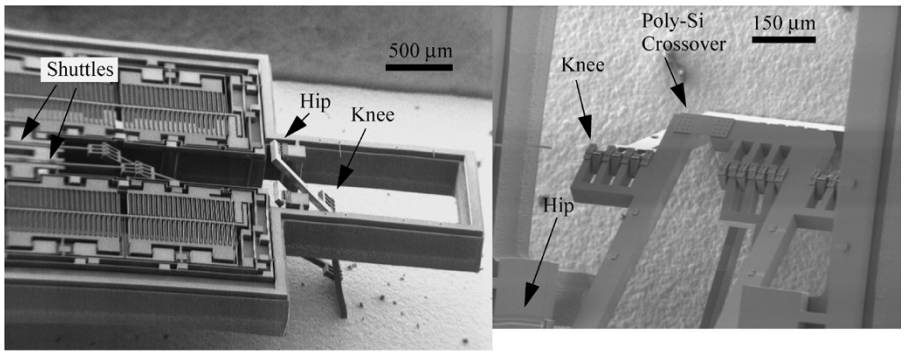

Fig. 20. (a) SEM of two-DOF leg. Leg is folded down touching the bottom of the die package. (b) SEM close-up of knee joint hinges comprise the joint connecting the legs and tendons together. Polysilicon cross-overs are used to bridge mechanical components. This enables us to design out-of-plane multi-DOF devices.

to a point, and then decreases. As the clutch voltage increases, the peak of the force curve shifts to the right, indicating the peak force is at a larger drive voltage. This pattern indicates that the inchworm motor's force output is limited by the clutch's ability to engage the shuttle. The limiting factor is when the clutch teeth physically slip against the shuttle teeth as is the case for lower clutch voltages. For low drive voltages, the force the leg can exert is limited by the force the drive actuators can produce. At very high drive voltages, the degree of clutch-shuttle slipping increases and thus the leg's output force decreases. As the clutch actuation voltage increases, however, the clutch engagement strength increases, increasing the peak force which the leg can exert.

Because of the design of the robot in [21], however, the robot operates at a 50 V drive and 50 V clutch voltage placing it at the lower end of the force curve in Fig. 19. Without clutch/shuttle slipping, the force output should be on the order of 400 μN, a distant cry from the forces we have previously measured. We have not determined the cause of the clutch/shuttle slipping. One possibility involves the geometry of the teeth and how that affects the engagement force. Future fabrication runs could include design variations of both the teeth geometry and the clutch actuator. Tooth designs that had deeper insets and were slightly angled could change the contact angle of the shuttle and clutch. A contact angle perpendicular to the shuttle could reduce the force against the clutch and consequently the frequency of slipping.

D. Two-DOF Leg

We also fabricated a 2-DOF leg operated with the same external controller (Fig. 20). The segmented leg is 1 mm in total length and driven by two electrostatic inchworm motors. The entire device measures $6 \times 3\ \mathrm{mm}^2$. Each joint was exercised with at least 90° of static angular deflection. The area swept out by the foot of the leg is more than $0.1\ \mathrm{mm}^2$. Each inchworm motor was designed for and has demonstrated a shuttle displacement of 400 μm with speeds up to 6.8 mm/s, a 70% improvement over previously reported results [24]. At this shuttle speed, the leg experiences an angular velocity of $1530°/\mathrm{s}$. The inchworm motor was driven using a 40 V drive and 50 V clutch actuation voltage. Reversing the leg motion was accomplished using the scheme outlined as Method 1 above. Reverse operation tests yielded nearly identical speeds to forward operation. In forward operation, the foot of the leg has exerted from 6 to 33 μN of vertical force, depending on the angle of the joints. The leg exerted larger forces the more it was deflected out of the plane. Shallower leg angles saw correspondingly lower forces.

In the first attempt to drive the robot leg, only a few steps at a time were possible before the clutch would slip against the shuttle. After running the inchworm motors a few dozen times, however, the shuttle would become more and more "unstuck," where finally the legs operated reliably without noticeably slipping. Further, endurance tests have shown that the leg is visually undamaged and continued to operate normally after 60 000 full leg sweeps for 16.5 h of operation (~10 million inchworm cycles).

IX. Conclusions and Future Work

A sticking point in the successful fabrication of microrobots was the lack of processes available which combine out-of-plane actuation with large force and efficient actuators. This process redresses this issue. Key here is the recognition that high force actuators can be attained from ASE/Bosch high-aspect-ratio etches resulting in large topographical variations on the surface of the wafer. The ability to planarize on top of this surface allows us to do standard polysilicon micromachining (i.e., hinge fabrication). While we chose a reflowed-glass technology to achieve this goal, other possibilities can include TEOS conformal oxide, oxidation growth to fill in deep trenches, or even silicon fusion bonding.

Once we established the viability of basic mechanical components in the SOI/poly process (hinges, sliders, motors, wiring) we were able to look at the design from a higher, more conceptual viewpoint. However, we needed to understand the dynamics associated with inchworms and contact friction to better design legs. With that said, we were able to evaluate sidewall etch effects on the performance of the motors and include a basic estimate for polysilicon/single-crystalline silicon contact forces.

In demonstrating leg motion with considerable output force, we can look farther down the research road toward even better performing legs and ultimately better performing microrobots. The legs themselves suffer in yield through contaminants

shorting out electrical contacts, undesired bubbles, and hinges breaking, though over the course of the process development, we have been able to significantly improve on yield. Furthermore, measured leg force was limited to about one-fifth of the calculated force for reasons related to gear teeth slipping in the inchworm motor. We believe with a modest amount of work these issues could be further worked out.

Last, this process ultimately served as the vehicle to making the frame, legs, and motors of the solar powered robot. However, in the SOI/poly process, other devices are possible, too. A large design space is available to transform a planar design into a 3-D structure using both the SOI device layer and the polysilicon layers as structural elements. We could imagine designing a high force three-DOF manipulator or an array of two-DOF micromirrors. Ultimately, though, our eyes are set on microrobots, and we see this work as being one step closer to the goal of achieving multi-DOF, multilegged microrobots.

ACKNOWLEDGMENT

The authors would like to thank C. Keller from MEMS Precision Instruments (http://www.mem-spi.com), University of California, Berkeley Microlab, especially B. Hamilton and J. Donnelly, J. Wu from Lawrence Livermore Labs, and D. Kousminov from Accurel Systems.

REFERENCES

[1] R. S. Fearing, "Powering 3 dimensional microrobots: power density limitations," in *Tutorial on Micro Mechatronics and Micro Robotics, ICRA*, 1998.

[2] M. Gebhard and W. Benecke, "Microtechnologies for microscaled robots and components," in *Proc. 1995 INRIA/IEEE Symp. Emerging Technologies and Factory Automation (ETFA'95)*, vol. 3, Paris, France, Oct. 1995, pp. 9–20.

[3] D. Wood, J. S. Burdess, and A. J. Harris, "Actuators and their mechanisms in microengineering," *Eng. Sci. Education J.*, vol. 7, no. 1, pp. 19–27, Feb. 1998.

[4] J. Yan, R. J. Wood, S. Avadhanula, M. Sitti, and R. S. Fearing, "Development of PZT and PZN-PT based unimorph actuators for micromechanical flapping mechanisms," in *IEEE Int. Conf. Robot. Automat.*, Seoul, Korea, May 21–26, 2001, pp. 3839–3846.

[5] P. Dario *et al.*, "Review microactuators for microrobots: a critical survey," *J. Micromech. Microeng.*, vol. 2, pp. 141–157, 1992.

[6] T. Ebefors, J. U. Mattsson, E. Kalvesten, and G. Stemme, "A walking silicon micro-robot," in *Proc. 10th Int. Conf. Sens. Actuators (Transducers '99)*, Sendai, Japan, Jun. 7–10, 1999, pp. 1202–1205.

[7] R. Yeh, E. J. J. Kruglick, and K. S. J. Pister, "Surface-micromachined components for articulated microrobots," *J. Microelectromech. Syst.*, vol. 5, no. 1, pp. 10–17, Mar. 1996.

[8] M. F. Pai and N. C. Tien, "Low voltage electrothermal vibromotor for silicon optical bench applications," *Sens. Actuators A, Phys.*, vol. 83, no. 1–3, pp. 237–243, May 2000.

[9] H. N. Kwon, S. H. Jeong, S. K. Lee, and J. H. Lee, "Design and characterization of a micromachined inchworm motor with thermoelastic linkage actuators," *Sens. Actuators A, Phys.*, vol. 103, no. 1–2, p. 143, 2003.

[10] J. M. Maloney, D. S. Schreiber, and D. L. DeVoe, "Large-force electrothermal linear micromotors," *J. Micromech. Microeng.*, vol. 14, pp. 226–234, 2004.

[11] S. Konishi, K. Ohno, and M. Munechika, "Parallel linear actuator system with high accuracy and large stroke," *Sens. Actuators A, Phys.*, vol. 97–98, pp. 610–619, 2002.

[12] M. Mita, M. Arai, S. Tensaka, D. Kobayashi, and H. Fujita, "A micromachined impact microactuator driven by electrostatic force," *J. Microelectromech. Syst.*, vol. 12, no. 1, p. 37, Feb. 2003.

[13] N. R. Tas, T. Sonnenberg, R. Molenaar, and M. Elwenspoek, "Design, fabrication and testing of laterally driven electrostatic motors employing walking motion and mechanical leverage," *J. Micromech. Microeng.*, vol. 13, no. 1, pp. N6–N15, Jan. 2003.

[14] N. Tas, J. Wissink, L. Sander, T. Lammerink, and M. Elwenspoek, "Modeling, design and testing of the electrostatic shuffle motor," *Sens. Actuators A, Phys.*, vol. 70, no. 1–2, pp. 171–178, Oct. 1998.

[15] M. P. de Boer, D. L. Luck, W. R. Ashurst, R. Maboudian, A. D. Corwin, J. A. Walraven, and J. M. Redmond, "High performance surface-micromachined inchworm actuator," *J. Microelectromech. Syst.*, vol. 13, no. 1, pp. 63–74, Feb. 2004.

[16] K. S. J. Pister, M. W. Judy, S. R. Burgett, and R. S. Fearing, "Microfabricated hinges," *Sens. Actuators A, Phys.*, vol. A33, no. 3, pp. 249–56, Jun. 1992.

[17] K. Suzuki, I. Shimoyama, H. Miura, and Y. Ezura, "Creation of an insect-based microrobot with an external skeleton and elastic joints," in *Proc. IEEE Workshop MEMS 1992*, Travemunde, Germany, Feb. 4–7, 1992, pp. 190–195.

[18] R. Yeh, E. J. J. Kruglick, and K. S. J. Pister, "Surface-micromachined components for articulated microrobots," *J. Microelectromech. Syst.*, vol. 5, no. 1, pp. 10–17, Mar. 1996.

[19] P. E. Kladitis and V. M. Bright, "Prototype microrobots for micro-positioning and micro-unmanned vehicles," *Sens. Actuators A, Phys.*, vol. 80, pp. 132–137, 2000.

[20] A. A. Yasseen, J. D. Cawley, and M. Mehregany, "Thick glass film technology for polysilicon surface micromachining," *J. Microelectromech. Syst.*, vol. 8, no. 2, pp. 172–179, Jun. 1999.

[21] S. Hollar, A. Flynn, C. Bellew, and K. S. J. Pister, "Solar powered 10 mg silicon robot," in *MEMS 2004*, Kyoto, Japan, January 19–23, 2004.

[22] H. Jiang, K. Yoo, J. A. Yeh, Z. Li1, and N. C. Tien, "Fabrication of thick silicon dioxide sacrificial and isolation blocks in a silicon substrate," *J. Micromech. Microeng.*, vol. 12, pp. 87–95, 2002.

[23] S. Hollar, S. Bergbreiter, and K. S. J. Pister, "Two-DOF robot leg operation and reversible inchworm motors," in *Transducers 2003*, Boston, MA, Jun. 2003.

[24] R. Yeh, S. Hollar, and K. S. J. Pister, "Single mask, large force, and large displacement electrostatic linear inchworm motors," *J. Microelectromech. Syst.*, vol. 11, no. 4, pp. 330–336, Aug. 2002.

[25] R. Yeh and K. S. J. Pister, "Measurement of static friction in mechanical couplings of articulated microrobots," in *Proc. SPIE*, Austin, TX, 1995, pp. 40–50.

[26] Robot Leg Videos, S. Hollar. (2004, Mar.). [Online]. Available: http://www-bsac.eecs.berkeley.edu/archive/users/hollar-seth/

[27] C. G. Keller, private communication, Jan. 2004.

Seth Hollar received the B.S. degree in electrical engineering from the Massachusetts Institute of Technology (MIT), Cambridge, in 1996, and the Ph.D. degree in mechanical engineering from the University of California, Berkeley (UCB), in 2003.

Currently, he is a Visiting Fellow at the Research and Development Center, Toshiba Corporation, Kawasaki, Japan. His research interests include microrobotics and system-level MEMS design and integration.

Anita Flynn received the B.S., the M.S., and the Ph.D. degrees in electrical engineering and computer science from the Massachusetts Institute of Technology (MIT), Cambridge, in 1983, 1985, and 1995, respectively.

From 1985 to 1990, she was a Research Scientist in the Mobile Robotics Group, MIT Artificial Intelligence Laboratory, Cambridge. Between 1995 and 1997, she was a Lecturer and Post-Doctoral Associate at the Electrical Engineering and Computer Science Department, University of California, Berkeley (UCB). During 1999–2000 academic year, she was a Visiting Assistant Professor at the Mechanical Engineering Department at UCB. She is now a President of MicroPropulsion Corporation, Oakland, CA. She is engaged in research in microrobotics.

Sarah Bergbreiter (S'04) received the B.S.E. degree in electrical engineering from Princeton University, Princeton, NJ, in 1999, and the M.S. degree in electrical engineering from the University of California, Berkeley, in 2004. Currently, she is pursuing the Ph.D. degree in electrical engineering with a focus on MEMS and robotics, at the same university.

Her research interests are in microrobotics, large-scale multirobot systems, and sensor networks.

Kristofer S. J. Pister received the B.S. degree in applied physics from the University of California, San Diego (UCSD), in 1986, and the M. S. and the Ph.D. degrees in electrical engineering from the University of California, Berkeley (UCB), in 1989 and 1992, respectively.

From 1992 to 1997, he was an Assistant Professor of Electrical Engineering at the University of California, Los Angeles (UCLA), where he helped develop graduate MEMS curriculum. Since 1996, he has been a Professor of Electrical Engineering and Computer Sciences at UCB. In 2003 and 2004, he was on leave from UCB. During that time, he was a CEO and then CTO of Dust Networks, a company he founded to commercialize Smart Dust. The last 18 years of his academic career have been spent in pursuit of millimeter-scale robots. His research efforts have yielded few robots but several commercially viable technologies including nodal CAD for MEMS, xenon difluoride etching, and wireless sensor networks. He has participated in many government science and technology programs, including the Defense Advanced Research Project Agency's Innovative Space Based Radar Antenna Technology project (DARPA's ISAT) and Defense Science Study Groups. He is currently a member of the Jasons. His research interests include MEMS, micro robotics, and low power circuits.